A procedure to model and design elastomeric-based isolation systems for the seismic protection of rocking art objects

Davide Pellecchia, Stefania Lo Feudo, Nicolò Vaiana, Jean-Luc Dion, Luciano Rosati

DOI: 10.1111/mice.12775

ORIGINAL ARTICLE

COMPUTER-AIDED CIVIL AND INFRASTRUCTURE ENGINEERING WILEY

A procedure to model and design elastomeric-based isolation systems for the seismic protection of rocking art objects

Davide Pellecchia[1] | **Stefania Lo Feudo**[2] | **Nicolò Vaiana**[1] | **Jean-Luc Dion**[2] | **Luciano Rosati**[1]

[1] Department of Structures for Engineering and Architecture, University of Naples Federico II, Naples, Italy

[2] QUARTZ (EA7393), VAST-FM, ISAE SUPMECA, Institut Supérieur de Mécanique de Paris, Saint-Ouen, France

Correspondence
Nicolò Vaiana, Department of Structures for Engineering and Architecture, University of Naples Federico II, 80125 Naples, Italy.
Email: nicolo.vaiana@unina.it

Present address
Nicolò Vaiana, via Claudio 21, 80125 Naples, Italy.

[Correction added on 23 October 2021 after first online publication: few formatting issues are fixed in the equations]

Abstract

This paper investigates the rocking behavior of rigid bodies seismically protected by means of lead rubber bearings and high damping rubber bearings, which are the most popular kinds of elastomeric isolators in the market. The complex nonlinear force–displacement relationship displayed by such devices is predicted by a phenomenological model based on a small set of parameters having a clear mechanical meaning. The algebraic nature of the proposed hysteretic model makes it suitable for a design procedure, using an energy-based approach, that allows one to obtain the hysteretic model parameters on the basis of the mass and the isolation period. Overturning spectra are evaluated and discussed to illustrate the effect of the isolation devices on the rigid bodies' rocking behavior. Furthermore, nonlinear time history analyses associated with six real earthquakes are carried out on six of Michelangelo's sculptures, located in the *Galleria dei Prigioni* at the Accademia Gallery of Florence, in order to examine their actual behavior under real strong ground motions.

1 | INTRODUCTION

Over the past years, new concepts and techniques have been developed for protecting structures from earthquakes and severe winds (Gutierrez Soto & Adeli, 2017; Naeim & Kelly, 1999) on the basis of approaches exploiting passive (Andersson et al., 2015; Lin et al., 2010), semi-active, and active (Aldemir et al., 2012; Bitaraf et al., 2012; El-Khoury & Adeli, 2013; Gutierrez Soto & Adeli, 2018, 2019) control.

Though conceived mainly for buildings and bridges (Adeli & Kim, 2009; Ghaedi et al., 2017), such strategies have been also applied to the protection of the artwork collections against seismic events (Erdik et al., 2010).

Probably, the first research on the protection of museum objects from earthquake damage is that of Agbabian et al. (1990, 1991). The authors proposed to classify art objects and their supports, according to their shape and seismic behavior. Augusti et al. (1992) provided a few rules for the safeguard of art objects, such as allowing the sliding motion between the object and its support in order to reduce the inertia forces, lowering the object's center of mass to increase its stability, and provide the object with a base isolation system. From these studies, it appears that freestanding objects such as statues and amphorae are the most exposed elements. Indeed, when these objects are subjected to an earthquake, they can rock and consequently overturn.

After these preliminary studies, several further analyses have been conducted in the past decades on the rocking response of rigid bodies (Aslam et al., 1978; Housner, 1963; Ishiyama, 1982; Taniguchi, 2002; Yim et al., 1980; Zhang & Makris, 2001; Zuccaro et al., 2017). Although this is a well-known topic in the scientific literature, there have been many recent and significant developments, such as the derivation of closed-form solutions (Kounadis, 2015), the investigation on the role of the friction coefficient (Gesualdo et al., 2016; Gesualdo, Iannuzzo, Minutolo, & Monaco, 2018; Gesualdo, Iannuzzo, Monaco, & Penta, 2018), the influence of heavy masses on the rocking behavior (Gesualdo, Iannuzzo, & Monaco, 2018), the assessment of the existing protocols for shake table testing of freestanding objects (D'Angela et al., 2021), and the study of the seismic response of storage racks (Malhotra, 2009). From the experimental point of view, recent researches aim at determining the friction coefficients between the rigid body and the base (Monaco et al., 2014) and the minimum horizontal acceleration required to activate rocking (Berto et al., 2021).

In the field of vibrations passive control, many papers focused on the study of the seismic protection of rigid bodies by means of a base isolation system modeled as a linear viscoelastic element (Caliò & Marletta, 2003; Contento & Di Egidio, 2009; Di Egidio & Contento, 2009; Roussis & Odysseos, 2014; Roussis et al., 2008). The use of mass-damper dynamic absorbers (Di Egidio et al., 2019), as well as rate-dependent or rate-independent hysteretic energy dissipation devices (Makris & Aghagholizadeh, 2019), were also studied. Other studies have been dedicated to active (Di Egidio, Contento, Olivieri, & de Leo, 2020; Simoneschi et al., 2018; Venanzi et al., 2018) and semi-active (Ceravolo et al., 2016, 2017) control systems to prevent the rocking of rigid bodies.

Contento and Di Egidio (2014) investigated the seismic protection of freestanding rigid bodies placed on a multi-floor with the base isolation modeled as a linear viscoelastic element. Kavvadias et al. (2019) focused on the seismic mitigation of a statue, modeled as a rigid body, placed on the top floor of a two-story reinforced concrete frame building. The authors considered two cases of base isolation, both with the friction pendulum sliding bearings as isolation devices. In the former case, the base isolation was applied to the building, whereas in the latter, the base isolation was implemented on the base of the statue.

Sorace and Terenzi (2015) and Sorace et al. (2016) focused on museums with floor isolation systems. The double-friction pendulum isolators were used for the base-isolated floor, whereas the museum contents were modeled with a finite element approach. Siami et al. (2018) investigated the effect of coupling two inerters to the isolation system of Michelangelo's *Pietà Rondanini*. The base isolation was made by rubber bearings and friction slides and was realized to protect the famous statue during a relocation in another museum and to preserve it from earthquakes and environmental vibrations. The isolation acts in both horizontal and vertical directions. Furthermore, the dynamical characteristics of typical statue-pedestal systems have been studied by Wittich and Hutchinson (2016).

In the previous studies, much attention was given to the friction pendulum sliding bearings, with a single or double concave surface (Baggio et al., 2015, 2018; Berto et al., 2013; Kavvadias et al., 2017; Roussis & Odysseos, 2017; Vassiliou & Makris, 2012), whereas the elastomeric isolators did not receive the same attention, although it represents one of the most popular isolation systems. For example, these devices are used for the protection of some statues, such as the Greek bronze statue of the *Dancing Satyr*, made in the Hellenistic period and on display at the *Dancing Satyr Museum* (Mazara del Vallo, Italy), and the Roman bronze statue of the *Emperor Germanico* made in the 1st century AD and exposed at the archaeological Museum *Edilberto Rosa* (Amelia, Italy; Caliò & Marletta, 2004). Vestroni and Cinto (2000) proposed to endow the statues with laminated rubber bearings. The statue was modeled as a single-degree-of-freedom system although the rocking behavior was not explored.

Concerning the design of the base isolation systems, a typical procedure is the selection from the seismic design spectra of a target period for the isolated structure leading to an admissible base shear or peak response (Ahmad et al., 2020; Eltahawy et al., 2018). On the other hand, in the case of a freestanding statue, the main objective of the isolation system is to prevent overturning and rocking. Therefore, the performance of an isolation system can be estimated by means of the overturning spectra, which depicts the amplitude of an impulsive excitation leading to the body overturning versus its circular frequency. It has been shown by Ther and Kollár (2018) that overturning induced by seismic events can be accurately predicted under an impulsive excitation with proper duration and peak acceleration. Notably, the variation of the maximum rocking angle with respect to a geometrical property of the block under seismic excitation can be displayed by the rocking maps (Di Egidio, Contento, de Leo, & Gardoni, 2020). The seismic risk assessment of a rigid body endowed with an isolation system can be also estimated by computing the fragility functions for a given engineering demand parameter (Jaimes & Candia, 2020; Thiers-Moggia & Málaga-Chuquitaype, 2019).

This paper focuses on the rocking behavior of rigid bodies and seismic protection of statues standing on an isolation base made by: (a) lead rubber bearings (LRBs) and (b) high damping rubber bearings (HDRBs), which are the main categories of elastomeric isolators. The hysteretic

response of the isolation system is modeled by means of an accurate uniaxial phenomenological model belonging to a class formulated by Vaiana et al. (2018), thus greatly improving the accuracy of the dynamic response of this highly nonlinear coupled system. The parameters of the proposed hysteretic model have a mechanical meaning clearer than those characterizing the differential model used in some of the above-mentioned works (Makris & Aghagholizadeh, 2019; Roussis & Odysseos, 2017; Vassiliou & Makris, 2012; Vestroni & Cinto, 2000). In addition, we propose a new design process using an energy-based approach regarding the above-mentioned hysteretic model. Especially, we exploit the hysteretic model's algebraic nature to derive a formula that computes the energy dissipated per cycle by a closed-form expression. This can be particularly useful from a technical point of view. The design procedure consists of evaluating the small number of models parameters by a constrained optimization problem, equating the energies dissipated by a linear viscous system and an elastomeric isolator. In this way, the model parameters have been established on the basis of specific and clear criteria, in contrast to the majority of further hysteretic models, mostly the Bouc–Wen one, in which they are directly provided without justifying their values and the procedure used to obtain them.

In the analyses, we consider two collapse conditions that could occur, namely, overturning of the rigid body and the failure of isolation devices when the horizontal displacement reaches the admissible displacement of the elastomeric isolator. The last condition sheds light on an important issue: If we decide to isolate a rocking object, it could collapse from the failure of the isolation device if the value of the impulse-to-rigid body angular frequency ratio is conveniently high.

The paper is organized as follows. The system under investigation, namely, the base-isolated rigid body is presented in Section 2, outlining its geometrical properties, its kinematics, the equations of motion, and the formulation of the collisions. The main characteristics of two kinds of elastomeric isolators, namely, the LRBs and the HDRBs, are briefly presented in Section 3 with particular emphasis on the description of their hysteretic behavior. In Section 4, the general class of hysteretic models formulated by Vaiana et al. (2018) and the uniaxial phenomenological model able to reproduce the behavior of the elastomeric bearings (Vaiana et al., 2019a) is summarized. In Section 5, we present the design procedure able to predict the mechanical characteristics of the isolators using an energy-based approach. In Section 6, the performances of the elastomeric bearings-based isolation under impulsive excitation are assessed with the aid of overturning spectra. Finally, the results obtained from the analyses applied to the six of Michelangelo's sculptures located in the *Galleria dei Prigioni* at the Accademia Gallery of Florence subjected to six different earthquakes are shown and discussed. The conclusions of the research are drawn in Section 7.

2 | MODEL SETTING

The system here studied is composed of a rigid body simply supported on an isolation base. The following assumptions have been made: The rigid body is symmetric with respect to the vertical axis and has uniform density; accordingly, the center of mass is on the vertical axis of symmetry. Furthermore, as usual in the specialized literature, a 2D model has been assumed. The sliding motion is prevented (Dimitrakopoulos & Paraskeva, 2015; Linde et al., 2020; Petrone et al., 2017) either by assuming that the kinetic friction between the rigid body and the isolation base is sufficiently high or supposing that there are some constraints able to prevent the relative horizontal displacement between the rigid body and the isolation base. This model has already been explored in the scientific literature (e.g., see Vassiliou & Makris, 2012).

The rigid body has mass m and polar inertia about rotation axis through its center of mass I_{cm}. Denoting as O and O', the centers of rotation, that is, the two bottom corners of the rigid body, the horizontal and vertical distances between O $[O']$ and the center of mass are b and h, respectively (see Figure 1). Consequently, the radial distance between the center of rotation and the center of mass is equal to $R = \sqrt{b^2 + h^2}$, and the polar inertia about the rotation axis through one of the two centers of rotation is $I_O = I_{\mathrm{cm}} + m R^2$. When the rigid body is at rest, the radial distance R forms an angle $\alpha = \tan^{-1}(b/h)$ with the vertical axis, this is a measure of the body slenderness.

The isolation base has mass m_b and it is connected to the support through elastomeric isolators. The isolators' vertical stiffness was considered far greater than the horizontal one. Consequently, rotation and curvilinear translation of the base are neglected.

2.1 | Kinematics and equations of motion

Based on the previous assumptions, the system has two degrees of freedom: one relative to the rocking motion of the rigid body, and the other corresponds to the relative translation motion of the isolation base. Nevertheless, depending on the behavior of the system, the two degrees of freedom are not both activated. Notably, there are two phases of motion: (a) full-contact motion in which the rigid body is in contact with the isolation base; (b) rocking motion in which the rigid body rocks around one of the two centers of rotation while the isolation base moves horizontally.

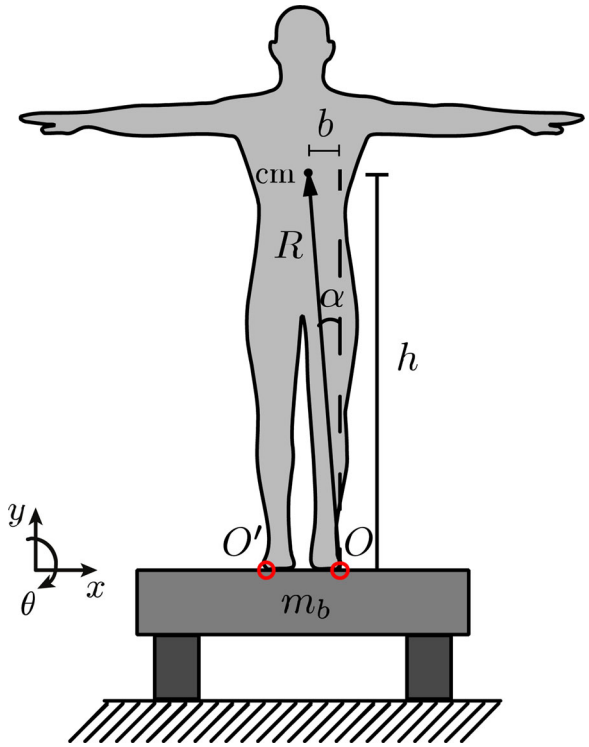

FIGURE 1 Geometrical properties of the seismically base-isolated rigid body

The Lagrangian parameters that describe the two above-mentioned kinds of motions are the relative displacement between the isolation base and the ground $u(t)$ and tilting of the rigid body $\theta(t)$. According to Newton's notation, their first and second derivatives with respect to the time are denoted as $\dot{u}(t), \dot{\theta}(t)$ and $\ddot{u}(t), \ddot{\theta}(t)$, respectively.

The horizontal component of the base acceleration acting on the fixed support is denoted as $\ddot{u}_g(t)$. Unless otherwise specified, the dependence on time will be omitted hereafter.

An xy coordinate system has been defined to establish the positive directions of displacements, velocities, and accelerations (see Figure 1). The positive direction of x due right and that of y is upward; finally, we assume that clockwise rotations around the reference frame's origin turn have a positive magnitude.

The equations of motion change according to the kind of motion that the rigid body undergoes. Consequently, in the next subsections, we outline the starting condition as well as the equations of motion for each phase.

2.2 | Full-contact

In the full-contact phase, the rigid body has one degree of freedom described by the Lagrangian parameter u. This phase occurs when both initial conditions in terms of angular displacement and velocity are null ($\theta_0 = 0$ and $\dot{\theta}_0 = 0$) and when the starting condition of the rocking phase is unsatisfied. The latter will be detailed in the next section.

The equation of motion that describes the full-contact phase can be obtained by applying Newton's second law of linear motion and balancing all forces acting on the body in the horizontal direction (see Figure 2a)

$$(m + m_b)\left(\ddot{u}_g + \ddot{u}\right) + n_d f = 0 \tag{1}$$

where n_d denotes the number of elastomeric isolators, and f represents the elastomeric device restoring force.

The full-contact phase stops when the rocking phase starts.

2.3 | Rocking

Both Lagrangian parameters, namely, u and θ, are activated in the rocking phase. Since the rigid body is symmetric, it is possible to take into account the change of the sign in θ, that is, when the body changes the center of rotation, by means of the signum function sgn(·). Accordingly, the starting condition, as well as the equations of motion, are valid when rigid body rocks either around the left or around the right corner.

The rocking phase can start when the overturning moment due to the inertial forces is greater than the resisting moment due to the gravity acceleration g, namely, $|\ddot{u}_g + \ddot{u}| > g\, b/h$, or for $\theta_0 \neq 0$, and/or $\dot{\theta}_0 \neq 0$.

The equations of motion can be obtained by applying Newton's second law of both linear and angular motion and balancing all horizontal forces and moments acting on the body (see Figure 2b):

$$m\left(\ddot{u}_g + \ddot{u} + \ddot{u}_\theta\right) + m_b\ \left(\ddot{u}_g + \ddot{u}\right) + n_d f = 0 \tag{2a}$$

$$I_O\ddot{\theta} + m\ \left(\ddot{u}_g + \ddot{u}\right) R\ \cos\left(\mathrm{sgn}\left(\theta\right)\alpha - \theta\right) = -m\ g\ R\ \sin\left(\mathrm{sgn}\left(\theta\right)\alpha - \theta\right) \tag{2b}$$

where $\ddot{u}_\theta$ is the second derivative with respect to the time of the horizontal displacement u_θ of the center of mass of the rigid body with respect to the isolation base.

The rocking phase ends when the angular velocity vanishes after a collision, that is, $|\dot{\theta}| = 0$.

2.4 | Collisions

When the angular displacement θ approaches zero, the rigid body collides with the isolation base, with a sudden change in its motion. For inelastic collisions, the kinetic energy of the system and the body velocity decrease.

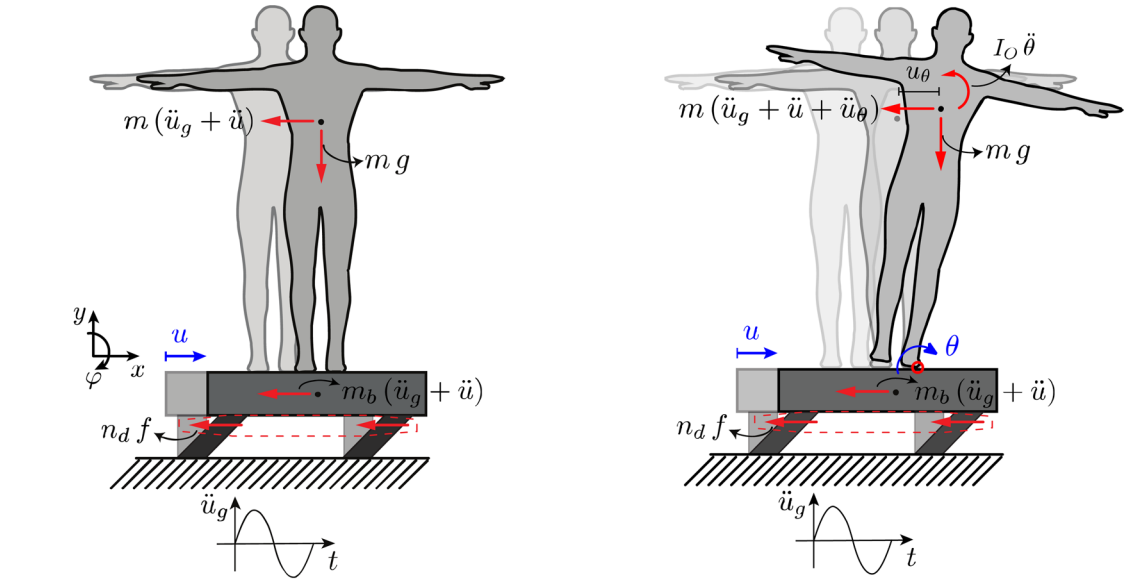

FIGURE 2 Instances of the motion that can occur: (a) full-contact, (b) rocking

Being the statue a slender body, we assume that after the collision, the body can only re-uplift by changing the center of rotation, that is, there is no bouncing of the body on the corner in contact (Caliò & Marletta, 2003).

To obtain the initial condition immediately after the collision, the law of conservation of linear [angular] momentum is used. In fact, although the kinetic energy decreases, the linear [angular] momentum remains unchanged. The subscript $(\cdot)_i$ will denote the pre-collision quantities, whereas the subscript $(\cdot)_f$ will identify the post-collision quantities.

Conservation of angular momentum on bottom corner O gives

$$I_O\ \dot{\theta}_i - 2mbR\sin(\alpha)\,\dot{\theta}_i + mR\ \cos(\alpha)\,\dot{u}_i = I_O\dot{\theta}_f + mR\cos(\alpha)\,\dot{u}_f \tag{3}$$

and the conservation of linear momentum of the entire system along the horizontal direction gives:

$$(m + m_b)\ \dot{u}_i + m\ \dot{u}_{\theta_i} = (m + m_b)\ \dot{u}_f + m\,\dot{u}_{\theta_f} \tag{4}$$

Taking the derivative of u_θ with respect to the time and replacing it in Equation (4), we obtain

$$(m + m_b)\,\dot{u}_i + mR\cos(\alpha)\ \dot{\theta}_i = (m + m_b)\ \dot{u}_f + mR\cos(\alpha)\,\dot{\theta}_f \tag{5}$$

In conclusion, the angular and linear velocities after the collision can be obtained by solving Equations (3) and (5) for the variables $\dot{\theta}_f$ and $\dot{u}_f$. Accordingly

$$\dot{\theta}_f = \left(1 + \frac{2b^2 m}{h^2 m\tilde{m} - I_O}\right)\dot{\theta}_i \tag{6}$$

and

$$\dot{u}_f = \dot{u}_i\ - \frac{2\,b^2\,h\,m\,\tilde{m}}{h^2\,m\,\tilde{m} - I_O}\,\dot{\theta}_i \tag{7}$$

where $\tilde{m} = m/(m + m_b)$.

Provided that the rocking phase ceases after a collision, Equations (6) and (7) are written as follows:

$$\dot{\theta}_f = 0 \tag{8a}$$

$$\dot{u}_f = \dot{u}_i\ + \tilde{m}\,R\cos(\alpha)\ \dot{\theta}_i \tag{8b}$$

in which the Equation (8b) trivially follows from Equation (5) with $\dot{\theta}_f = 0$.

3 | ELASTOMERIC ISOLATORS

Elastomeric isolators are one of the most popular types of isolation devices used for seismic protection. They have a circular or square cross-section and are made of alternating layers of rubber and thin steel plates that are bonded together by a specific manufacturing process. The reinforcing elements prevent the lateral expansion of the elastomer

due to the axial compressive load, whereas the elastomer material provides energy dissipation and flexibility.

The main categories of elastomeric bearings for seismic isolation applications are the low damping rubber bearings, HDRBs, and LRBs (Losanno, Hadad, & Serino, 2019; Losanno, Spizzuoco, & Calabrese, 2019; Losanno et al., 2020; Naeim & Kelly, 1999). The formers are typically used in coupling with other kinds of isolators (e.g., flat sliders, steel yielding devices, and viscous dampers) due to their limited damping capacity. Consequently, in this section, we analyze the differences only between HDRBs and LRBs, with a particular emphasis on the force-transverse displacement ($f - u$) relationship.

3.1 | LRBs

The LRBs are generally characterized by one lead cylinder inserted in a vertical hole into the rubber bearings. The lead cylinder increases the horizontal stiffness in order to limit the horizontal displacements produced by the non-seismic horizontal loads, as well as the energy dissipation capacity. Therefore, the initial tangent stiffness of these devices is approximately 10 times the post-elastic tangent stiffness, and the equivalent viscous damping factor can reach a value up to $\xi = 15 - 35\%$ (Naeim & Kelly, 1999). Several dynamic tests conducted on these kinds of devices show that at strains approaching 200%, there is no stiffening behavior so that the force–displacement hysteretic loop is bounded between two parallel straight lines (Tyler & Robinson, 1984; see Figure 3a).

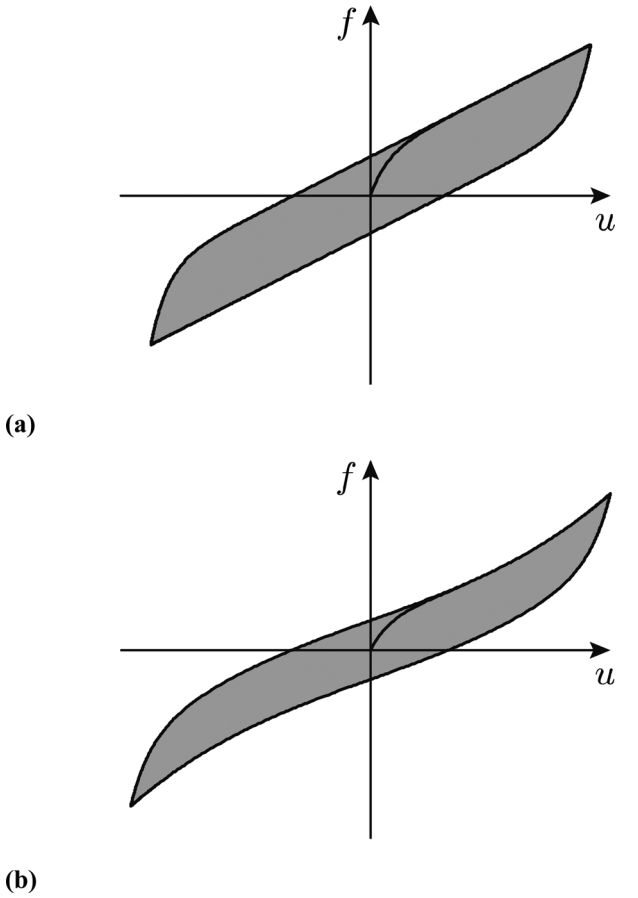

FIGURE 3 Typical hysteretic loops displayed by the main categories of elastomeric bearings for seismic isolation applications: (a) lead rubber bearings (LRBs); (b) high damping rubber bearings (HDRBs)

3.2 | HDRBs

The HDRBs allow one to reach an equivalent viscous damping factor of $\xi = 10 - 20\%$ at a shear strain of $\gamma = 100\%$. The shape of the HDRB's force–displacement relationship depends on the value of the applied shear strain. Notably, the shear modulus at low levels of shear strain ($\gamma < 100\%$) can be five times greater than the one at shear strain levels of $\gamma \approx 100 - 150\%$ (Constantinou et al., 2007). For relatively small values of shear strain, namely, $\gamma \leq 100 - 150\%$, the hysteretic loop is bounded between two parallel straight lines. As the shear strain increases ($\gamma > 100 - 150\%$), a stiffening behavior is shown (Fujita et al., 1990), and consequently the HDBR's hysteretic loop is bounded between two parallel curves (see Figure 3b).

4 | HYSTERETIC MODEL

To reproduce the complex nonlinear behavior typical of most seismic isolators, it is important to use an accurate model. To this end, the Bouc–Wen model (Bouc, 1971; Wen, 1976) is the most popular hysteretic model and is used to simulate several types of hysteretic phenomena (Ikhouane et al., 2007; Ismail et al., 2009). This model is of differential nature, that is, the equation that allows one to evaluate the output state variable is a nonlinear ordinary differential equation. Unfortunately, this differential equation could need some iterative techniques for each time step of the nonlinear time history analysis by increasing the computational costs. To overcome the limits of the differential models, we use a computationally efficient model belonging to a class developed by Vaiana et al. (2018). This model is of algebraic nature so that it is possible to evaluate the output variable in closed form. Consequently, the computation time for geometrically and mechanically nonlinear dynamics analyses can be reduced. Moreover, this model can be used in a design procedure using an energy-based approach (described in Section 5) since it is possible to evaluate the dissipated energy analytically.

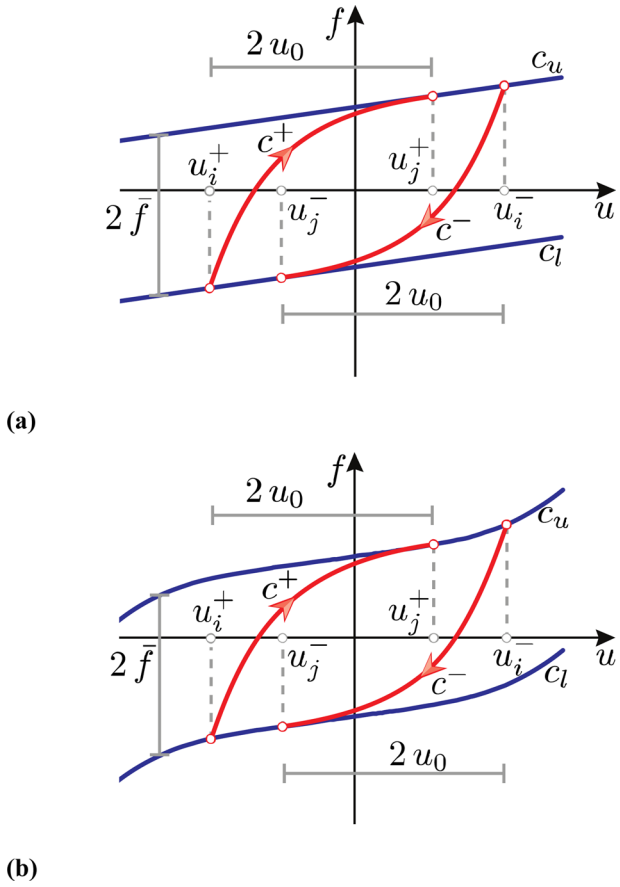

FIGURE 4 Hysteresis loop bounded by two straight parallel lines (a) or curves (b)

4.1 | Assumptions of the class of hysteretic models

First of all, the class of hysteretic models is able to reproduce a symmetric loop bounded between two parallel straight lines (Figure 4a) or curves (Figure 4b). Additionally, it assumes that the general loop is defined by four separate curves:

- the upper and the lower limiting curves, denoted as c_u and c_l, respectively, and represented by the blue color in Figure 4;
- the loading and unloading limiting curves, denoted as c^+ and c^-, respectively, and represented in red in Figure 4.

As shown in Figure 4, the model assumes that the distance between the upper and the lower limiting curves is constant and equal to $2\,\bar{f}$, in which $\bar{f}$ $[-\bar{f}]$ represents the point of intersection between the upper [lower] limiting curve with the axis of ordinate. This assumption implies that the distance between the starting and the ending point on the upper [lower] limiting curves c_u $[c_l]$, denoted as u_i and u_j, respectively, is assumed to be constant and equal to $2\,u_0$ (see Figure 4). Accordingly, utilizing the superscript $+$ $[-]$ to denote the generic loading [unloading] curve, one obtains $u_i^+ = u_j^+ - 2\,u_0$ $[u_i^- = u_j^- + 2\,u_0]$. Note that if the restoring force is equal for positive and negative excitations, the displacements u_j^+ $[u_i^+]$ and u_j^- $[u_i^-]$ can be the same in absolute value.

Consequently, in the generic loading case, that is to say, when the horizontal velocity is positive ($\dot{u} > 0$), the generalized force f is computed as

$$f\left(u, u_j^+\right) = \begin{cases} c^+\left(u, u_j^+\right) & \text{if } u \in \left[u_j^+ - 2u_0, u_j^+\right] \\ c_u\left(u\right) & \text{if } u \in \left[u_j^+, \infty\right) \end{cases} \tag{9}$$

Conversely, for a generic unloading case ($\dot{u} < 0$), the generalized force f can be computed in the following way

$$f\left(u, u_j^-\right) = \begin{cases} c^-\left(u, u_j^-\right) & \text{if } u \in \left[u_j^-, u_j^- + 2u_0\right] \\ c_l\left(u\right) & \text{if } u \in \left(-\infty, u_j^-\right] \end{cases} \tag{10}$$

4.2 | Elastomeric bearings formulation

The model described in Vaiana et al. (2019a) to simulate the behavior of the LRBs and HDRBs has been adopted in this paper. Consequently, the reader is asked to refer to the above-mentioned reference for a more comprehensive description and further details. The expressions of the upper (lower) and the loading (unloading) limiting curves for elastomeric isolators are

$$c_u = \beta_1 u^3 + \beta_2\, u^5 + k_b\, u + \bar{f} \tag{11a}$$

$$c_l = \beta_1 u^3 + \beta_2\, u^5 + k_b\, u - \bar{f} \tag{11b}$$

and

$$c^+ = \beta_1\ u^3 + \beta_2 u^5 + k_b\, u + \bar{f} + (k_a - k_b)\left(\frac{\left(1+u-u_j^+ + 2\,u_0\right)^{(1-\lambda)}}{1-\lambda} - \frac{(1+2\,u_0)^{(1-\lambda)}}{1-\lambda}\right) \tag{12a}$$

$$c^- = \beta_1\ u^3 + \beta_2 u^5 + k_b\, u - \bar{f} + (k_a - k_b)\left(\frac{\left(1-u+u_j^- + 2\,u_0\right)^{(1-\lambda)}}{\lambda-1} - \frac{(1+2\,u_0)^{(1-\lambda)}}{\lambda-1}\right) \tag{12b}$$

where u represents the longitudinal displacement and k_a, k_b, λ, β_1, and β_2 are the model parameters. In particular,

k_a is the tangent stiffness of curve c^+ [c^-], at $u = u_i^+$ [$u = u_i^-$], k_b is the tangent stiffness of curve c^+ [c^-] at $u = u_j^+$ [$u = u_j^-$], and the dimensionless parameter λ defines the rate of change of the tangent stiffness from k_a to k_b for both curves c^+ and c^-. Finally, the parameters β_1, and β_2 define the curvatures of the upper and lower limiting curves. From a mathematical point of view, $k_a > k_b$, $k_a > 0, \lambda > 0, \lambda \neq 1 >, u_0 > 0$, and $\beta_1, \beta_2 \in \mathbb{R}$.

The internal model parameters u_0 and $\bar{f}$ can be evaluated as follows:

$$u_0 = \frac{1}{2}\left[\left(\frac{k_a - k_b}{\delta_k}\right)^{\frac{1}{\lambda}} - 1\right] \tag{13}$$

$$\bar{f} = \frac{k_a - k_b}{2}\left(\frac{(1+2u_0)^{(1-\lambda)} - 1}{1-\lambda}\right) \tag{14}$$

in which δ_k is the difference between the two values assumed by the tangent stiffness at u_j^+ [u_j^-] and it may be set equal to 10^{-20} as explained in Vaiana et al. (2019a).

5 | THE ENERGY-BASED DESIGN PROCESS FOR THE DEFINITION OF THE HYSTERETIC MODEL PARAMETERS

The above-mentioned model parameters (k_a, k_b, λ, β_1, β_2) can be calibrated from experimental testing by an inverse identification strategy as shown in Sessa et al. (2020). However, this approach could be a hard task for the designer since the experimental data of elastomeric isolators are not available on the manufacturers' catalogs. Hence, the choice of the mechanical characteristics of the elastomeric isolators, and consequently the isolator's type and size, could require some iterations in the design process.

This section provides a design procedure able to predict the parameters of the algebraic hysteretic model described in Section 4 that is strictly related to the mechanical characteristics of the elastomeric isolators. This procedure is based on equating the area of the hysteresis loop with the shape of an ellipse, which represents the energy dissipated through the equivalent linear rate-dependent hysteretic model and the area of the hysteresis loop displayed by an elastomeric isolator. In this way, the hysteretic model parameters can be evaluated from data easily available to the designer, namely, the isolated system's mass and period, the admissible displacement of the elastomeric device, and the viscous damping factor.

5.1 | Evaluation of the energy dissipated per cycle

The force–displacement relationship is an ellipse when the damping is strictly viscous. The area of the ellipse represents the energy dissipated and it is computed as follows:

$$E_v = 2\pi\, k_{\text{eff}}\, u_{\max}^2\, \xi \tag{15}$$

where k_{eff} is the effective secant stiffness of the peak-to-peak values in the hysteresis loop, $u_{\max}$ is the maximum displacement, and ξ is the viscous damping factor.

The energy dissipated by the hysteresis loop in one cycle, simulated through the algebraic hysteretic model, can be evaluated in closed form, owing to the fact that each curve of the hysteresis loop is defined by analytical expressions. Indeed, the energy dissipated on the interval $[-u_{\max}, u_{\max}]$ is the difference between the area below the top and the bottom curve of the loop, that is:

$$E_h = E_h^t - E_h^b = \left(\int_{-u_{\max}}^{-u_{\max}+2u_0} c^+\, \mathrm{d}u + \int_{-u_{\max}+2u_0}^{u_{\max}} c_u\, \mathrm{d}u\right) - \left(\int_{-u_{\max}}^{u_{\max}-2u_0} c_l\, \mathrm{d}u + \int_{u_{\max}-2u_0}^{u_{\max}} c^-\, \mathrm{d}u\right) \tag{16}$$

so that replacing Equations (11a,11b) and (12a,12b) in the previous equation, one obtains

$$E_h = \frac{(1+2u_0)^{-\lambda}}{(\lambda-2)(\lambda-1)}\Big[2(k_a - k_b)(1+2u_0)(1+2u_0(\lambda-1)) - 2(1+2u_0)^{\lambda}\left(k_a - k_b - 2\bar{f}\, u_{\max}(\lambda-2)(\lambda-1)\right)\Big] \tag{17}$$

We infer from Equation (17), that the dissipated energy E_h does not depend on the model parameters β_1 and β_2. In fact, the hysteresis loop is symmetric, that is, it is characterized by an odd function with respect to the origin of the reference frame; consequently, the variation of curvature of the limiting curves c_u and c_l does not affect the area of the hysteresis loop.

The initial tangent stiffness k_a can be expressed as a multiple of the post yield tangent stiffness k_b

$$k_a = \eta\, k_b \tag{18}$$

where η is the initial-to-post yield tangent stiffness ratio (Naeim & Kelly, 1999; Skinner et al., 1993). Naeim and Kelly (1999) recommended $\eta \approx 3 - 6$ for the HDBRs and $\eta \approx 10 - 21$ for the LRBs.

Replacing Equations (13), (14), and (18) in Equation (17), we get

$$E_h = \frac{2}{(\lambda-2)(\lambda-1)}\left\{k_b(\eta-1)(u_{\max}(\lambda-2)-1) + \lambda\left(\frac{k_b(\eta-1)}{\lambda}\right)^{\frac{1}{\lambda}}\left[(\lambda-1)\left(\frac{k_b(\eta-1)}{\lambda}\right)^{\frac{1}{\lambda}} - (\lambda-2)(u_{\max}+1)\right]\right\} \tag{19}$$

5.2 | Evaluation of the hysteretic model parameters

The algebraic hysteretic model's area depends on just two parameters, namely, k_b and λ, once the initial-to-post yield tangent stiffness ratio η and the admissible displacement of the elastomeric isolator $u_{\max}$ have been established. These mechanical characteristics can be estimated by means of a constrained optimization problem obtained by equating the energy dissipated by the hysteresis loop simulated through the algebraic hysteretic model E_h and the equivalent viscous one E_v.

In this way, the effective secant stiffness k_{eff} in Equation (15) can be evaluated from the properties of the seismically base-isolated rigid body, that is,

$$k_{\text{eff}} = \left(\frac{2\pi}{T_{bi}}\right)^2 (m+m_b) \tag{20}$$

in which T_{bi} and $m+m_b$ are the isolation period and the total mass, respectively.

Let us define the objective function to be optimized ϵ as the relative error between the energy dissipated by the equivalent viscous model and the algebraic hysteretic model,

$$\epsilon = \frac{|E_v - E_h|}{|E_v|} \tag{21}$$

The constrained optimization problem consists of minimizing the function ϵ with respect to the variables k_b and λ and in the presence of constraints on those variables. Accordingly, the problem can be expressed in the following form

$$\min_{\substack{k_b\in\mathbb{R}^+\setminus\{0\}\\ \lambda\in\mathbb{R}^+\setminus\{0,1\}}} \epsilon(k_b,\lambda) \quad \text{subject to} \quad k_b = k_{\text{eff}} - \frac{\bar{f}}{u_{\max}} \tag{22}$$

wherein the constraint $k_b = k_{\text{eff}} - \bar{f}/u_{\max}$ is nonlinear given the dependence of $\bar{f}$ on the unknowns k_b and λ (see Equation 14).

The problem (22) has to be solved numerically. In this study, we used the interior point technique (for a more extensive description, see Waltz et al., 2006).

In order to provide the best estimate of the optimal solution, it is necessary to define the initial points k_b^0 and λ_0. A general criterion for a correct choice of k_b^0 and λ_0 does not exist. However, the extensive numerical tests that have been carried out by the authors, starting with randomly generated initial points, have proved that the values

$$k_b^0 = k_{\text{eff}} \quad \text{and} \quad \lambda^0 = \frac{\log\left(\frac{k_{\text{eff}}(\eta-1)}{\delta_k}\right)}{\log(1+2u_{\max})} \tag{23}$$

provide a good lower local minimum objective function value. The order of magnitude of the relevant value at solution is equal to 10^{-10}.

The expression of λ^0 has been obtained by inverting Equation (13) and setting $k_b^0 = k_{\text{eff}}$ and $u_0 = u_{\max}$.

6 | NUMERICAL EXPERIMENTS

In this section, we show the results of some numerical analyses performed on rigid bodies seismically isolated by means of the two kinds of elastomeric isolators described in Section 3. The strongly nonlinear force–displacement relationship displayed by the elastomeric isolators has been simulated through the algebraic hysteretic model described in Section 4. The parameters of the hysteretic model have been computed by the energy-based design procedure described in Section 5. The analyses consider two collapse conditions that could occur, namely, overturning of the rigid body when tilt angle reaches 90 degrees $|\theta| = \pi/2$ (Di Egidio & Contento, 2009; Ishiyama, 1982), and the failure of isolation devices when the horizontal displacement reaches the admissible displacement of the elastomeric isolator $|u| = u_{\max}$.

6.1 | Overturning spectra generated by impulsive excitation

First of all, the overturning spectra (Di Egidio et al., 2019; Vassiliou & Makris, 2012; Zhang & Makris, 2001) have been evaluated in order to establish the performance of the two kinds of elastomeric isolators in the protection of a rigid body subjected to an impulsive excitation. These spectra are obtained for rigid bodies having the geometrical and dynamical properties presented in Table 1, where α, m, and

TABLE 1 Properties of the rigid body used for generating the overturning spectra

α (deg)	m (kg)	m_b (kg)	ω_r (rad s^{-1})
15	5 000	286.20	Var.

TABLE 2 Properties of the elastomeric isolators

			ξ (%)		η (–)	
n_d	T_{bi} (s)	$u_{\max}$ (m)	LRB	HDRB	LRB	HDRB
4	2	0.30	15	15	10	5

m_b are detailed in Section 2, whereas $\omega_r = \sqrt{m\,g\,R/I_O}$ is the fundamental angular rocking frequency of the rigid body.

The system is subjected to an impulsive signal with a shape of a full sine cycle $\ddot{u}_g = A_{\ddot{u}_g} \sin(\omega_{\ddot{u}_g} t)$ where $A_{\ddot{u}_g}$ is the magnitude, supposed to be a variable, and $\omega_{\ddot{u}_g}$ is the angular frequency, supposed to be equal to $2\,\pi/0.5$ rad s^{-1}.

The evaluation of the algebraic model parameters for simulating the elastomeric isolators' hysteresis loops by means of the design procedure defined in Section 5 requires the definition of the following properties: the number of the elastomeric isolators, the isolation period, the elastomeric device's admissible displacement, the equivalent viscous damping factor, and the initial-to-post yield stiffness ratio. The selected values of properties for generating the overturning spectra are given in Table 2.

The algebraic model parameters for three types of elastomeric isolators, one LRB and two HDRBs, have been obtained by the design procedure and are reported in Table 3. Since the parameters β_1 and β_2 cannot be obtained from the design process, we assigned a value that provides stiffening behavior at a relatively large value of shear strain.

The overturning spectra in Figure 5 are shown by reporting on the abscissa the impulse-to-rigid body angular frequency ratio $\omega_{\ddot{u}_g}/\omega_r$, whereas there is the impulse magnitude normalized with the static value of the minimum overturning acceleration $A_{\ddot{u}_g}/(g\,\tan(\alpha))$ on the ordinate axis. Consequently, the filled contour maps are obtained by varying the impulse magnitude $A_{\ddot{u}_g}$ and the fundamental angular rocking frequency ω_r of the rigid body supported on: (a) no isolation system, (b) LRB, (c) HDRB$_1$, and (d) HDRB$_2$ isolation systems.

Color maps depict the maximum absolute value of the tilt angle $|\theta_{\max}|$ showing:

- the safe area—represented by the dark blue color—that is, the area in which the rigid body does not rock;
- the overturning area—represented by the red color—namely, the area where the rigid body overturns;
- the rocking area—represented by the colors between the dark blue and red color—that is, the area in which the rigid body rocks without overturning.

In addition, the spectra also consider the failure condition of the elastomeric isolators, represented by the 45 degrees parallel lines hatch pattern, that is, the area in which the elastomeric isolators fail due to the fact that the maximum horizontal displacement of the system exceeds the device's admissible displacement.

The comparison of the above-mentioned spectra highlights the performance of the elastomeric isolators. In fact, we can see that both kinds of base isolation increase the safe area, increasing as well the static value of the minimum overturning acceleration, in comparison to the spectrum of the non-isolated rigid bodies. However, we can also see that if the value of the impulse-to-rigid body angular frequency ratio $\omega_{\ddot{u}_g}/\omega_r$ is conveniently high, what typically happens for big-size bodies or high frequencies pulses, the collapse condition of the device will reduce the base-isolated rigid body's safe area in comparison to the non-isolated rigid body one.

The comparison between the spectra of the LRB and the HDRBs isolation systems shows significant differences. The safe area of the LRB isolation system's spectrum is wider than the ones related to the two HDRBs isolation systems. The increases of the minimum overturning acceleration of the two HDRBs isolation systems' spectra are less than those characterizing the LRB isolation system. Furthermore, the rocking area is prone to increase as the ratio $\omega_{\ddot{u}_g}/\omega_r$ increases when the rigid body is isolated by the HDRB$_1$ as well as HDRB$_2$ isolation systems.

From Figure 5c,d, we can compare the two HDRBs isolation systems. Figure 5c refers to an algebraic model in which the parameters β_1 and β_2 are equal to $\beta_1 = 50 \times 10^3$ N m^{-3} and $\beta_1 = 50 \times 10^3$ N m^{-5}, whereas in Figure 5d, the parameters β_1 and β_2 have been doubled, that is, $\beta_1 = 100 \times 10^3$ N m^{-3} and $\beta_1 = 100 \times 10^3$ N m^{-5}. This means that in the latter case, the stiffening behavior provides a restoring force of the device greater (in absolute value) than the former case, under the same displacement. Figure 5d shows that raising of the parameters β_1 and β_2 has the effect to reduce the safe area, given that the minimum overturning acceleration decreases, and in addition, the rocking area for high values of the ratio $\omega_{\ddot{u}_g}/\omega_r$ increases.

As regards the failure of the devices, it can be seen that for small values of the ratio $\omega_{\ddot{u}_g}/\omega_r$, the HDRBs devices reach displacements smaller than the LRB one. In addition, such displacements are prone to decrease with increasing values of β_1 and β_2. In order to establish a numerical quantification of the device failure condition, we denote with A_{LRB}, A_{HDRB_1}, and A_{HDRB_2}, the areas in which the LRB, HDRB$_1$, and HDRB$_2$

TABLE 3 The algebraic model parameters obtained by the energy-based design procedure

	k_b (N m^{-1})	λ (–)	β_1 (N m^{-3})	β_2 (N m^{-5})
Lead rubber bearing (LRB)	1.15×10^4	109.37	0	0
High damping rubber bearing 1 (HDRB$_1$)	1.14×10^4	46.70	50×10^3	50×10^3
High damping rubber bearing 2 (HDRB$_2$)	1.14×10^4	46.70	100×10^3	100×10^3

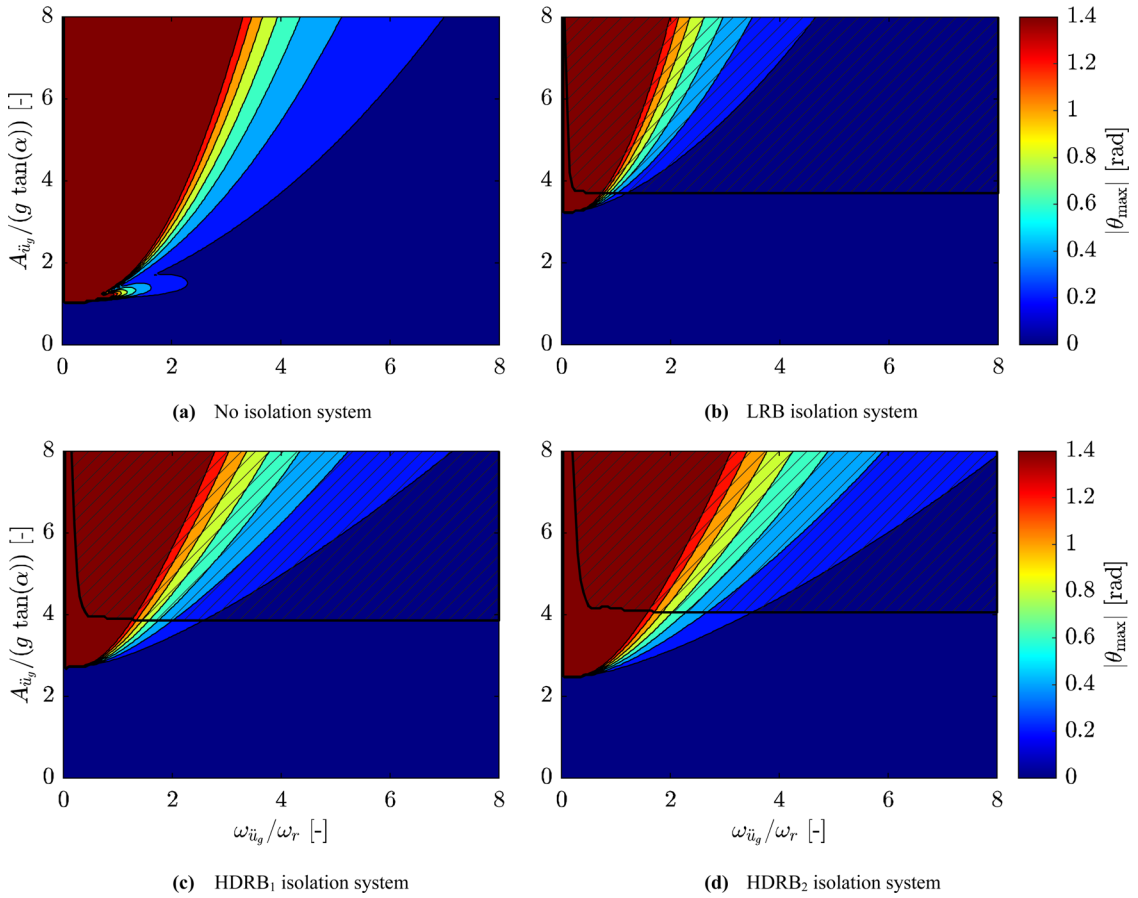

(a) No isolation system **(b)** LRB isolation system

(c) HDRB$_1$ isolation system **(d)** HDRB$_2$ isolation system

FIGURE 5 The overturning spectra for rigid bodies: without base isolation (a), isolated by the LRB (b), HDRB$_1$ (c), HDRB$_2$ (d) isolation systems defined in Table 3 and subjected to the full sine cycle. Dark blue color = safe area; red color = overturning area; further colors indicate rocking area; 45 degrees parallel lines hatch pattern indicates collapse area for elastomeric bearing

devices fail, respectively. Therefore, the ratios between the above-mentioned quantities are: $A_{LRB}/A_{HDRB_1} \approx 1.05$, $A_{LRB}/A_{HDRB_2} \approx 1.12$, and $A_{HDRB_1}/A_{HDRB_2} \approx 1.06$. Consequently, the HDRB's collapse area tends to decrease as the stiffening behavior increases, which happens if the β parameters are increased. Notably, the HDRB$_1$'s collapse area decreases by approximately 6% when doubling the β parameters.

6.2 | Application to sculptures subjected to seismic excitation

In this section, we examine the seismic response of six of Michelangelo's sculptures located in the *Galleria dei Prigioni* at the Accademia Gallery of Florence.

The geometrical properties of such statues, listed in Table 4, have been taken from Berto et al. (2012) who

TABLE 4 The geometrical properties (see Figure 1) of the equivalent blocks of the six of Michelangelo's sculptures located in the *Galleria dei Prigioni* at the Accademia Gallery of Florence (Berto et al., 2012)

	b (m)	h (m)	m (kg)
San Matteo	0.30	1.36	3 287
Pietà da Palestrina	0.39	1.26	7 084
Prigione che si Sveglia	0.32	1.41	5 644
Prigione il Giovane	0.36	1.28	4 005
Prigione Barbuto	0.37	1.29	4 655
Prigione Atlante	0.45	1.39	7 691

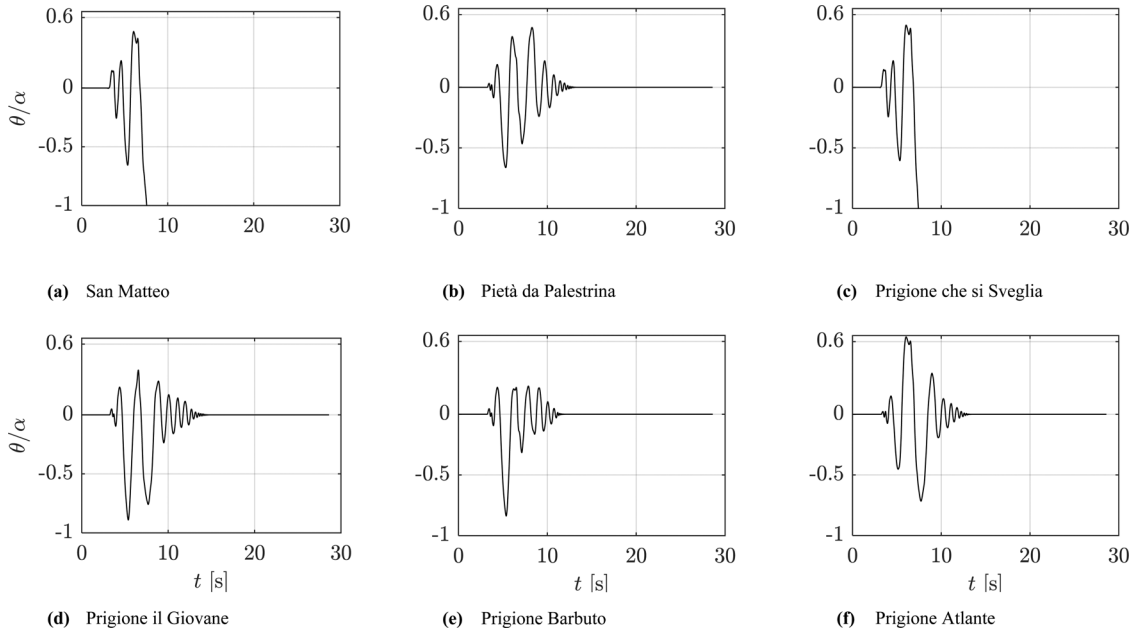

FIGURE 6 Rocking response of the Michelangelo's sculptures located in the *Galleria dei Prigioni* at the Accademia Gallery of Florence subjected to the horizontal ground acceleration recorded during the Northridge earthquake (1994)

performed the study of seismic assessment of art objects in museums supposing that the statues were equivalent to a prismatic block, named *equivalent block*. Although the symmetric model was quite reasonable for most of the statues, the above-mentioned authors concluded that the equivalent block model overestimates the stability capacity of the artifacts, compared to a more realistic model accounting for the eccentricities of the center of mass with respect to the centers of rotations (asymmetric model).

The masses listed in Table 4 are obtained supposing that the density of each statue was 2 650 kg m^{-3}.

Nonlinear time-history analyses have been conducted supposing that the mass of the isolated base m_b is the one shown in Table 1 and assuming the following seismic inputs:

- the strike parallel direction of the horizontal ground acceleration recorded at the Jensen Filter Plant station during the Northridge earthquake of January 17, 1994;
- the 000 component of the horizontal ground acceleration recorded at the Gilroy Array #1 station during the Loma Prieta earthquake of October 18, 1989;
- the 180 component of the horizontal ground acceleration recorded at the Geotech. Investig. Center station during the San Salvador earthquake of October 10, 1986;
- the East-West component of the horizontal ground acceleration recorded at the Gemona station during the Friuli earthquake of September 15, 1976;
- the North-South component of the horizontal ground acceleration recorded at the Mire station during the Emila earthquake of May 5, 2012.
- the North-South component of the horizontal ground acceleration recorded at the Domo station during the Central Italy earthquake of October 6, 2016.

First of all, we investigated the rocking behavior of the statues without the base isolation. Figure 6 displays the rocking angle θ normalized with respect to the angle α versus the time of each statue subjected to the Northridge earthquake. All statues rock and two of these, namely, *San Matteo* and *Prigione che si Sveglia*, overturn. The same conclusions are derived from the Central Italy earthquake. All statues rock without overturning when they are subjected to the Loma Prieta as well as the San Salvador earthquakes. Only *San Matteo* overturns due to the Friuli earthquake, while the remaining sculptures rock. The Emilia earthquake does not cause the overturning of the sculptures, even though the *San Matteo* and *Prigione che si Sveglia* statues rock. For completeness, we show in Figure 7 the results obtained for the *San Matteo* statue subjected to the above-mentioned seismic inputs. In any case, in addition to overturning, rocking is an unsatisfactory behavior because of the possible damages that the collisions cause with the pedestal (Di Sarno et al., 2015; Fragiadakis & Diamantopoulos, 2020; Konstantinidis & Makris, 2009). Consequently, all the statues need to be protected from seismic excitations.

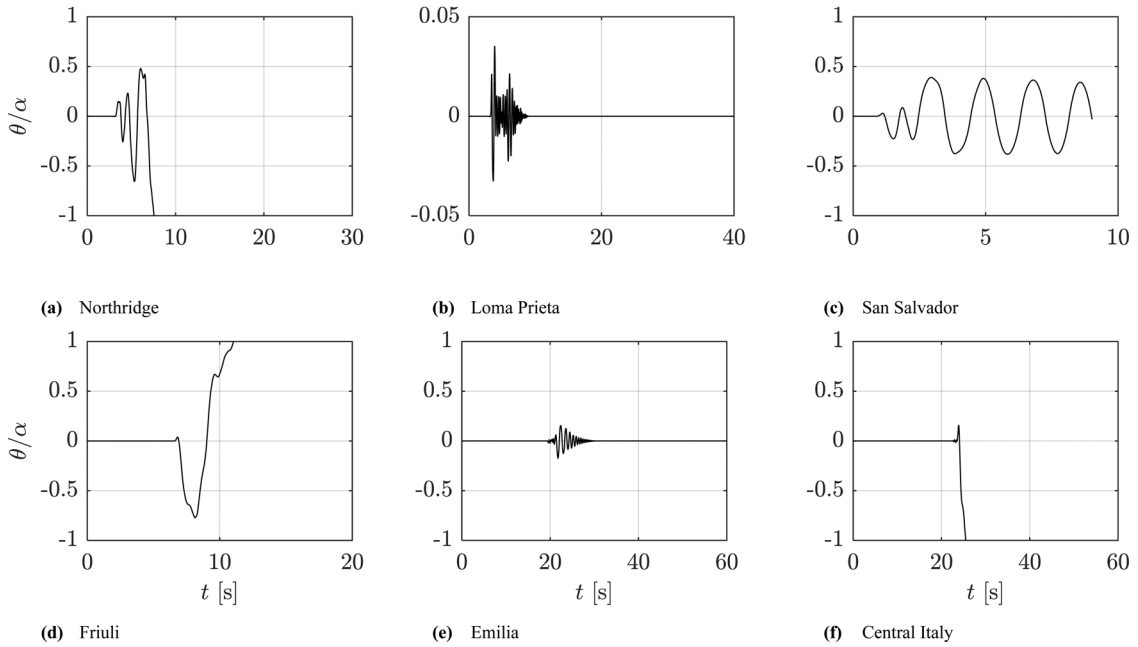

FIGURE 7 Rocking response of the *San Matteo* statue located in the *Galleria dei Prigioni* at the Accademia Gallery of Florence subjected to the: (a) Northridge, (b) Loma Prieta, (c) San Salvador, (d) Friuli, (e) Emilia, and (f) Central Italy seismic excitations

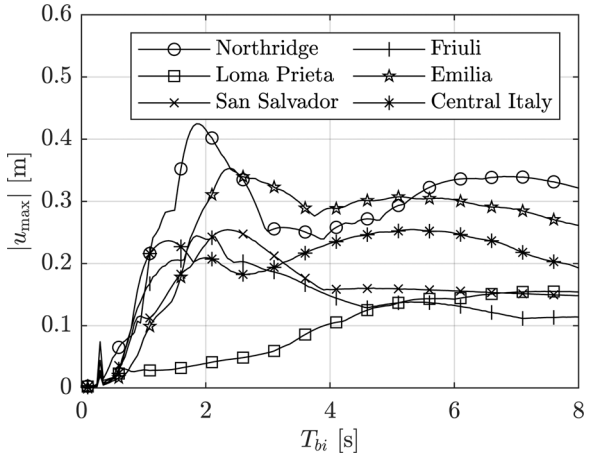

FIGURE 8 Full-contact spectra referring to the seismically base-isolated rigid body with four LRBs whose admissible displacement, viscous damping factor, and initial-to-post yield stiffness ratio are listed in Table 5

TABLE 5 The properties considered to evaluate the algebraic model parameters for the isolation of Michelangelo's sculptures with the LRBs

n_d	T_{bi} (s)	$u_{\max}$ (m)	ξ (%)	η (–)
4	3.7	0.30	15	10

Figure 8 shows the full-contact spectra regarding the seismically base-isolated rigid body with four LRBs, whose properties are listed in Table 5, and subjected to the six seismic excitations. The spectra are referred to one value of the viscous damping factor ξ, namely, 15% and depict the evolution of $|u_{\max}|$ with respect to the isolation period T_{bi}. The other properties of the LRBs, that is, the admissible displacement, and the initial-to-post yield stiffness ratio are reported in Table 2. We can see that lower values of the horizontal displacement are reached by choosing a value of the isolation period ranging from approximately 2.5 to 5.3 s. We chose $T_{bi} = 3.7$ s for further analyses (see Table 5).

TABLE 6 The algebraic model parameters obtained from the LRBs' properties listed in Table 5 by means of the energy-based design procedure

	k_b (N m^{-1})	λ (–)
San Matteo	2.26×10^3	109.37
Pietà da Palestrina	4.67×10^3	109.37
Prigione che si Sveglia	3.76×10^3	109.37
Prigione il Giovane	2.72×10^3	109.37
Prigione Barbuto	3.13×10^3	109.37
Prigione Atlante	5.05×10^3	109.37

The hysteretic model parameters have been obtained for each statue according to the above detailed design procedure and are reported in Table 6 where the parameters β_1 and β_2 have been omitted since they are null for the LRBs isolation system. The numerical results show that both collapse conditions, namely, the overturning of the statues and failure of the devices, are never attained. Moreover, all statues never rock and this avoids the possibility of damage due to impacts. For brevity, in Figure 9, we reported just the time-displacement relationships concerning the

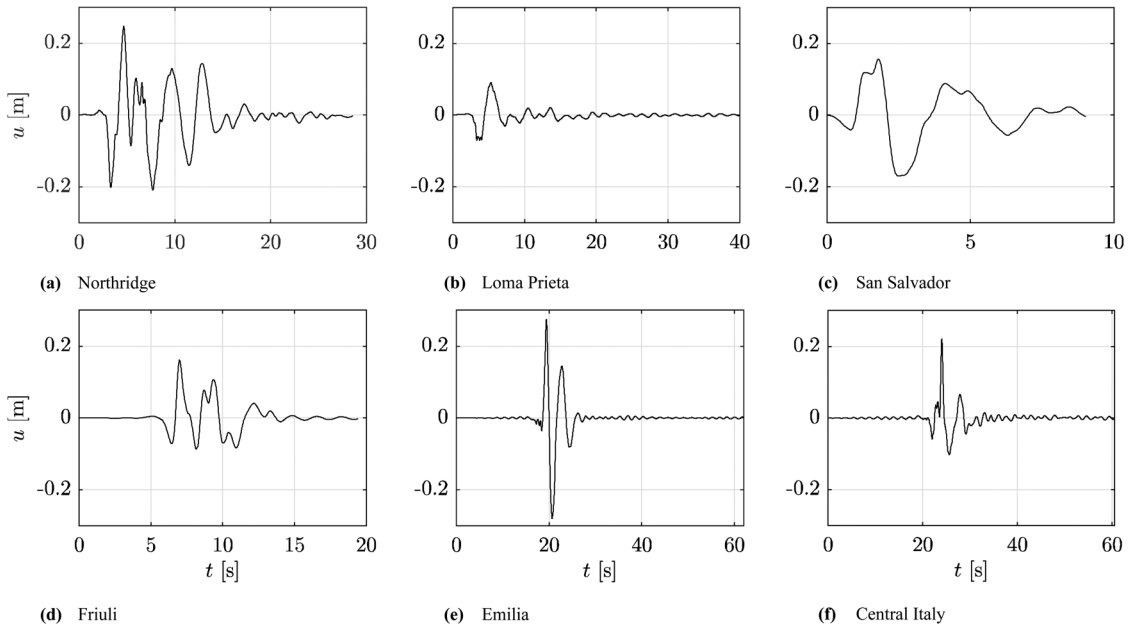

FIGURE 9 The displacement time histories of the seismically base-isolated rigid body with the LRBs isolation system, whose properties are listed in Table 5, subjected to the: (a) Northridge, (b) Loma Prieta, (c) San Salvador, (d) Friuli, (e) Emilia, and (f) Central Italy seismic excitations

TABLE 7 The properties considered to evaluate the algebraic model parameters for the isolation of the Michelangelo's sculptures with the HDRBs

n_d	T_{bi} (s)	$u_{\max}$ (m)	ξ (%)	η (–)
4	3.7	0.35	15	5

TABLE 8 The algebraic model parameters obtained from the HDRBs' properties listed in Table 7 by means of the energy-based design procedure

	k_b (N m^{-1})	λ (–)	β_1 (N m^{-3})	β_2 (N m^{-5})
San Matteo	2.25×10^3	40.16	1×10^4	1×10^4
Pietà da Palestrina	4.64×10^3	40.16	1×10^4	1×10^4
Prigione che si Sveglia	3.73×10^3	40.16	1×10^4	1×10^4
Prigione il Giovane	2.70×10^3	40.16	1×10^4	1×10^4
Prigione Barbuto	3.11×10^3	40.16	1×10^4	1×10^4
Prigione Atlante	5.02×10^3	40.16	1×10^4	1×10^4

six seismic excitations considered since the time-rocking angle relationships are always null for every statue.

The same analyses have been carried out considering the HDRBs devices as an isolation system. Table 7 presents the devices' properties providing the same results, in terms of the time-rocking angle relationship, of the LRB isolation. The related hysteretic model parameters obtained by the design procedure are listed in Table 8. For the sake of simplicity, we chose the same β_1 and β_2 parameters for all statues, although an ad hoc calibration for each statue would be needed in order to have stiffening behavior at a relatively large values of shear strain.

7 | CONCLUSION

In this work, the performance of the elastomeric bearings-base isolation in the protection of freestanding rigid bodies has been studied in depth. Particular emphasis was dedicated to the protection of art objects and, in particular, statues that require many stringent requirements for their protection. The paper examines the rocking behavior when the base isolation is supported on the main kinds of elastomeric isolators, that is, the LRBs and HDRBs. The complex hysteretic behavior displayed by such devices has been modeled by a uniaxial phenomenological model that offers many advantages. The model's validation and its accuracy have been proven in several papers (Vaiana et al., 2018, 2019a, 2019b). The model is based on a small set of parameters, directly associated with the mechanical properties of the device's hysteretic behavior to simulate. The model's algebraic nature and the mechanical meaning of the model parameters made it possible to define a new design procedure that allows one to obtain the hysteretic model parameters starting with some easily available properties, that is, the mass and the period of the system to isolate, the number, admissible displacement, viscous damping factor, and the initial-to-post yield tangent stiffness ratio of the elastomeric isolator. This design process exploits an energetic approach based on an equivalent viscous system.

The extensive numerical applications carried out show that the elastomeric bearings-base isolation increases the safe area in the overturning spectrum, that is, the area where the rigid body never rocks. The comparison between the LRB's overturning spectrum and the HDRB one shows that the former provides a safe area greater than the latter. Moreover, if the value of the impulse-to-rigid body angular frequency ratio is conveniently high, which typically happens for big-size bodies or high frequencies pulses, the collapse condition of the device reduces the base-isolated rigid body's safe area in comparison to the non-isolated rigid body one. Consequently, if we decide to isolate a rocking object, it could collapse for the failure of the isolation device. In addition, we compared the collapse area for both the LRB and the two HDRBs isolators.

The work presents also the results obtained with reference to six of Michelangelo's sculptures located in the *Galleria dei Prigioni* at the Accademia Gallery of Florence subjected to six earthquakes with pulse-like behavior. The full-contact spectrum of the isolated system under seismic excitations was computed to choose the isolation period, admissible displacement, and equivalent viscous damping of the devices. In this way, it has been possible to apply the design procedure in order to obtain the mechanical properties of the devices for each statue.

Both the LRB and the HDRB satisfied the assumed ultimate limit states, that is, no overturning, no breaking of the devices, and no rocking. Especially, the HDRB devices adopted to isolate the statues turned out to be less damped and more deformable than the LRB.

ACKNOWLEDGMENTS

The financial support of the Italian Ministry for University and Research - PON 2014-2020 (CUP: E66C18000940007, Code: DOT1318294), Fondo Sociale Europeo Azione I.1 "Dottorati Innovativi con caratterizzazione Industriale"; Project title: Technologies and applications for the conservation, management, and enhancement of cultural, artistic and landscape heritage, University of Naples Federico II Research Unit - is gratefully acknowledged.

ORCID

Davide Pellecchia https://orcid.org/0000-0003-2900-661X
Stefania Lo Feudo https://orcid.org/0000-0001-9158-5144
Nicolò Vaiana https://orcid.org/0000-0001-9890-3731
Jean-Luc Dion https://orcid.org/0000-0002-0124-9030
Luciano Rosati https://orcid.org/0000-0001-5072-9922

REFERENCES

Adeli, H., & Kim, H. (2009). *Wavelet-based vibration control of smart buildings and bridges*. CRC Press.

Agbabian, M. S., Ginell, W., Masri, S. F., & Nigbor, R. (1991). Evaluation of earthquake damage mitigation methods for museum contents. *Studies in Conservation*, *36*, 111–120.

Agbabian, M. S., Masri, S. F., Nigbor, R. L., & Getty Conservation Institute. (1990). Evaluation of seismic mitigation measures for art objects Getty seismic adobe project. *J. Paul Getty Trust.*

Ahmad, N., Shakeel, H., & Masoudi, M. (2020). Design and development of low-cost HDRBs seismic isolation of structures. *Bulletin of Earthquake Engineering*, *18*, 1107–1138.

Aldemir, U., Yanik, A., & Bakioglu, M. (2012). Control of structural response under earthquake excitation. *Computer-Aided Civil and Infrastructure Engineering*, *27*(8), 620–638.

Andersson, A., O'Connor, A., & Karoumi, R. (2015). Passive and adaptive damping systems for vibration mitigation and increased fatigue service life of a tied arch railway bridge. *Computer-Aided Civil and Infrastructure Engineering*, *30*(9), 748–757.

Aslam, M., Godden, W. G., & Scalise, D. T. (1978). *Earthquake rocking response of rigid bodies* (Tech. Rep. No. EERC 2003–07). Prepared for the Department of Energy under Contract W-7405-ENG-48.

Augusti, G., Ciampoli, M., & Airoldi, L. (1992). Mitigation of seismic risk for museum contents an introductory investigation. *Proceedings of 10th World Conference on Earthquake Engineering*, Madrid Spain (pp. 5995–6000).

Baggio, S., Berto, L., Favaretto, T., Saetta, A., & Vitaliani, R. (2015). Seismic isolation technique of marble sculptures at the Accademia Gallery in Florence: numerical calibration and simulation modelling. *Bulletin of Earthquake Engineering*, *13*(9), 2719–2744.

Baggio, S., Berto, L., Rocca, I., & Saetta, A. (2018). Vulnerability assessment and seismic mitigation intervention for artistic assets: from theory to practice. *Engineering Structures*, *167*, 272–286.

Berto, L., Favaretto, T., & Saetta, A. (2013). Seismic risk mitigation technique for art objects: experimental evaluation and numerical modelling of double concave curved surface sliders. *Bulletin of Earthquake Engineering*, *11*(5), 1817–1840.

Berto, L., Favaretto, T., Saetta, A., Antonelli, F., & Lazzarini, L. (2012). Assessment of seismic vulnerability of art objects: The Galleria dei Prigioni sculptures at the Accademia Gallery in Florence. *Journal of Cultural Heritage*, *13*(1), 7–21.

Berto, L., Meroi, E., Rocca, I., & Saetta, A. (2021). Rocking activation of free standing elements in real conditions: A safe experimentally-based acceleration limit. *Engineering Structures*, *226*(2), 111331.

Bitaraf, M., Hurlebaus, S., & Barroso, L. R. (2012). Active and semi-active adaptive control for undamaged and damaged building structures under seismic load. *Computer-Aided Civil and Infrastructure Engineering*, *27*(1), 48–64.

Bouc, R. (1971). Modèle mathématique d'hystérésis. *Acustica*, *24*(1), 16–25.

Caliò, I., & Marletta, M. (2003). Passive control of the seismic rocking response of art objects. *Engineering Structures*, *25*(8), 1009–1018.

Caliò, I., & Marletta, M. (2004). On the mitigation of the seismic risk of art objects: case-studies. *Proceedings of 13th World Conference on Earthquake Engineering*, British Columbia, Canada.

Ceravolo, R., Pecorelli, M. L., & Zanotti Fragonara, L. (2016). Semi-active control of the rocking motion of monolithic art objects. *Journal of Sound and Vibration*, *374*, 1–16.

Ceravolo, R., Pecorelli, M. L., & Zanotti Fragonara, L. (2017). Comparison of semi-active control strategies for rocking objects under pulse and harmonic excitations. *Mechanical Systems and Signal Processing*, *90*, 175–188.

Constantinou, M. C., Whittaker, A. S., Kalpakidis, Y., Fenz, D. M., & Warn, G. P. (2007). *Performance of seismic isolation hardware under service and seismic loading* (Technical Report No MCEER-07-0012). Multidisciplinary Center for Earthquake Engineering Research.

Contento, A., & Di Egidio, A. (2009). Investigations into the benefits of base isolation for non-symmetric rigid blocks. *Earthquake Engineering & Structural Dynamics*, *38*(7), 849–866.

Contento, A., & Di Egidio, A. (2014). On the use of base isolation for the protection of rigid bodies placed on a multi-storey frame under seismic excitation. *Engineering Structures*, *62–63*, 1–10.

D'Angela, D., Magliulo, G., & Cosenza, E. (2021). Towards a reliable seismic assessment of rocking components. *Engineering Structures*, *230*, 111673.

Di Egidio, A., Alaggio, R., Aloisio, A., de Leo, A. M., Contento, A., & Tursini, M. (2019). Analytical and experimental investigation into the effectiveness of a pendulum dynamic absorber to protect rigid blocks from overturning. *International Journal of Non-Linear Mechanics*, *115*, 1–10.

Di Egidio, A., & Contento, A. (2009). Base isolation of slide-rocking non-symmetric rigid blocks under impulsive and seismic excitations. *Engineering Structures*, *31*(11), 2723–2734.

Di Egidio, A., Contento, A., de Leo, A. M., & Gardoni, P. (2020). Dynamic and seismic protection of rigid-block-like elements and structures on deformable ground with mass-damper dynamic absorbers. *Journal of Engineering Mechanics*, *146*(6), 04020046.

Di Egidio, A., Contento, A., Olivieri, C., & de Leo, A. M. (2020). Protection from overturning of rigid block-like objects with linear quadratic regulator active control. *Structural Control and Health Monitoring*, *27*(10), e2598.

Di Sarno, L., Magliulo, G., D'Angela, D., & Cosenza, E. (2019). Experimental assessment of the seismic performance of hospital cabinets using shake table testing. *Earthquake Engineering & Structural Dynamics*, *48*(1), 103–123.

Dimitrakopoulos, E. G., & Paraskeva, T. S. (2015). Dimensionless fragility curves for rocking response to near-fault excitations. *Earthquake Engineering & Structural Dynamics*, *44*(12), 2015–2033.

El-Khoury, O., & Adeli, H. (2013). Recent advances on vibration control of structures under dynamic loading. *Archives of Computational Methods in Engineering*, *20*(4), 353–360.

Eltahawy, W., Ryan, K. L., Cesmeci, S., & Gordaninejad, F. (2018). Parameters affecting dynamics of threedimensional seismic isolation. *Journal of Earthquake Engineering*, *25*(4), 730–755.

Erdik, M., Durukal, E., Ertürk, N., & Sungay, B. (2010). Earthquake risk mitigation in istanbul museums. *Natural Hazards*, *53*(1), 97–108.

Fragiadakis, M., & Diamantopoulos, S. (2020). Fragility and risk assessment of freestanding building contents. *Earthquake Engineering & Structural Dynamics*, *49*(10), 1028–1048.

Fujita, T., Suzuki, S., & Fujita, S. (1990). High damping rubber bearings for seismic isolation of buildings (1st report. Hysteretic restoring force characteristics and analytical models). *Transactions of the Japan Society of Mechanical Engineers Series C*, *56*, 658–666.

Gesualdo, A., Iannuzzo, A., Guadagnuolo, M., Guerriero, A., Monaco, M., Savino, M., & Guadagnuolo, M. (2016). Numerical analysis of rigid body behaviour. *Applied Mechanics and Materials*, *847*, 240–247.

Gesualdo, A., Iannuzzo, A., Minutolo, V., & Monaco, M. (2018). Rocking of freestanding objects: Theoretical and experimental comparisons. *Journal of Theoretical and Applied Mechanics (Poland)*, *56*, 977–991.

Gesualdo, A., Iannuzzo, A., & Monaco, M. (2018). Rocking behaviour of freestanding objects. *Journal of Physics: Conference Series*, *1141*, 012091.

Gesualdo, A., Iannuzzo, A., Monaco, M., & Penta, F. (2018). Rocking of a rigid block freestanding on a flat pedestal. *Journal of Zhejiang University-SCIENCE A*, *19*(5), 331–345.

Ghaedi, K., Ibrahim, Z., Adeli, H., & Javanmardi, A. (2017). Recent developments in vibration control of building and bridge structures. *Journal of Vibroengineering (Invited Review)*, *19*(5), 3564–3580.

Gutierrez Soto, M., & Adeli, H. (2017). Recent advances in control algorithms for smart structures and machines. *Expert Systems*, *34*(2), e12205.

Gutierrez Soto, M., & Adeli, H. (2018). Vibration control of smart base-isolated irregular buildings using neural dynamic optimization model and replicator dynamics. *Engineering Structures*, *156*, 322–336.

Gutierrez Soto, M., & Adeli, H. (2019). Semi-active vibration control of smart isolated highway bridge structures using replicator dynamics. *Engineering Structures*, *186*, 536–552.

Housner, G. W. (1963). The behavior of inverted pendulum structures during earthquakes. *Bulletin of the Seismological Society of America*, *53*(2), 403–417.

Ikhouane, F., Mañosa, V., & Rodellar, J. (2007). Dynamic properties of the hysteretic Bouc-Wen model. *Systems & Control Letters*, *56*(3), 197–205.

Ishiyama, Y. (1982). Motions of rigid bodies and criteria for overturning by earthquake excitations. *Earthquake Engineering & Structural Dynamics*, *10*(5), 635–650.

Ismail, M., Ikhouane, F., & Rodellar, J. (2009). The hysteresis Bouc-Wen model, a survey. *Archives of Computational Methods in Engineering*, *16*(2), 161–188.

Jaimes, M. A., & Candia, G. (2020). Seismic risk of sliding ground-mounted rigid equipment. *Engineering Structures*, *204*, 110066.

Kavvadias, I., Bibo, H., & Vasiliadis, L. (2017). Numerical study on the dynamic response of classical column standing free on an isolated base. *Proceedings of 6th ECCOMAS Thematic Conference On Computational Methods in Structural Dynamics and Earthquake Engineering*, Rhodes Island, Greece.

Kavvadias, I., Vasiliadis, L., Elenas, A., & Koutsoupakis, K. (2019). Fragility assessment of base isolated free standing museum artifacts. *Proceedings of 6th Conference on Computational Methods in Structural Dynamics and Earthquake Engineering*, Limenas Chersonisou, Greece.

Konstantinidis, D., & Makris, N. (2009). Experimental and analytical studies on the response of freestanding laboratory equipment to earthquake shaking. *Earthquake Engineering & Structural Dynamics*, *38*(6), 827–848.

Kounadis, A. N. (2015). On the rocking sliding instability of rigid blocks under ground excitation: Some new findings. *Soil Dynamics and Earthquake Engineering*, *75*, 246–258.

Lin, C. -C., Chen, C. -L., & Wang, J. -F. (2010). Vibration control of structures with initially accelerated passive tuned mass dampers under near-fault earthquake excitation. *Computer-Aided Civil and Infrastructure Engineering*, *25*(1), 69–75.

Linde, S. A., Konstantinidis, D., & Tait, M. J. (2020). Rocking response of unanchored building contents considering horizontal and vertical excitation. *Journal of Structural Engineering*, *146*(9), 04020175.

Losanno, D., Hadad, H., & Serino, G. (2019). Design charts for eurocode-based design of elastomeric seismic isolation systems. *Soil Dynamics and Earthquake Engineering*, *119*, 488–498.

Losanno, D., Madera Sierra, I. E., Spizzuoco, M., Marulanda, J., & Thomson, P. (2020). Experimental performance of unbonded polyester and carbon fiber reinforced elastomeric isolators under bidirectional seismic excitation. *Engineering Structures*, *209*, 110003.

Losanno, D., Spizzuoco, M., & Calabrese, A. (2019). Bidirectional shaking-table tests of unbonded recycled-rubber fiber-reinforced bearings (rr-frbs). *Structural Control and Health Monitoring*, *26*(9), e2386.

Makris, N., & Aghagholizadeh, M. (2019). Effect of supplemental hysteretic and viscous damping on rocking response of free-standing columns. *Journal of Engineering Mechanics*, *145*(5), 04019028.

Malhotra, P. K. (2009). *Seismic analysis of structures and equipment*. Springer International.

Monaco, M., Guadagnuolo, M., & Gesualdo, A. (2014). The role of friction in the seismic risk mitigation of freestanding art objects. *Natural Hazards*, *73*(2), 389–402.

Naeim, F., & Kelly, J. M. (1999). *Design of seismic isolated structures: From theory to practice*. Wiley.

Petrone, C., Di Sarno, L., Magliulo, G., & Cosenza, E. (2017). Numerical modelling and fragility assessment of typical freestanding building contents. *Bulletin of Earthquake Engineering*, *15*(4), 1609–1633.

Roussis, P., & Odysseos, S. (2014). Slide-rocking response of seismically-isolated rigid structures subjected to horizontal ground excitation. *Proceedings of 2nd European Conference on Earthquake Engineering and Seismology*, Istanbul, Turkey.

Roussis, P., & Odysseos, S. (2017). Rocking response of seismically-isolated rigid blocks under simple acceleration pulses and earthquake excitations. *The Open Construction and Building Technology Journal*, *11*, 217–236.

Roussis, P., Pavlou, E., & Pisiara, E. (2008). Base-isolation technology for earthquake protection of art objects. *Proceedings of 14th World Conference on Earthquake Engineering*, Beijing, China.

Sessa, S., Vaiana, N., Paradiso, M., & Rosati, L. (2020). An inverse identification strategy for the mechanical parameters of a phenomenological hysteretic constitutive model. *Mechanical Systems and Signal Processing*, *139*, 106622.

Siami, A., Karimi, H. R., Cigada, A., Zappa, E., & Sabbioni, E. (2018). Parameter optimization of an inerter-based isolator for passive vibration control of Michelangelos Rondanini Pietà. *Mechanical Systems and Signal Processing*, *98*, 667–683.

Simoneschi, G., Olivieri, C., de Leo, A. M., & Di Egidio, A. (2018). Pole placement method to control the rocking motion of rigid blocks. *Engineering Structures*, *167*, 39–47.

Skinner, R. I., Robinson, W. H., & McVerry, G. (1993). *An introduction to seismic isolation.*. Wiley.

Sorace, S., & Terenzi, G. (2015). Seismic performance assessment and base-isolated floor protection of statues exhibited in museum halls. *Bulletin of Earthquake Engineering*, *13*(6), 1873–1892.

Sorace, S., Terenzi, G., Bitossi, C., & Mori, E. (2016). Mutual seismic assessment and isolation of different art objects. *Soil Dynamics and Earthquake Engineering*, *85*, 91–102.

Taniguchi, T. (2002). Non-linear response analyses of rectangular rigid bodies subjected to horizontal and vertical ground motion. *Earthquake Engineering & Structural Dynamics*, *31*(8), 1481–1500.

Ther, T., & Kollár, L. P. (2018). Overturning of rigid blocks for earthquake excitation. *Bulletin of Earthquake Engineering*, *16*, 1607–1631.

Thiers-Moggia, R., & Málaga-Chuquitaype, C. (2019). Seismic protection of rocking structures with inerters. *Earthquake Engineering & Structural Dynamics*, *48*(5), 528–547.

Tyler, R. G., & Robinson, W. H. (1984). High-strain tests on lead-rubber bearings for earthquake loadings. *Bulletin of the New Zealand Society for Earthquake Engineering*, *17*(2), 90–105.

Vaiana, N., Sessa, S., Marmo, F., & Rosati, L. (2019b). Nonlinear dynamic analysis of hysteretic mechanical systems by combining a novel rate-independent model and an explicit time integration method. *Nonlinear Dynamics*, *98*(4), 2879–2901.

Vaiana, N., Sessa, S., Marmo, F., & Rosati, L. (2018). A class of uniaxial phenomenological models for simulating hysteretic phenomena in rate-independent mechanical systems and materials. *Nonlinear Dynamics*, *93*(3), 1647–1669.

Vaiana, N., Sessa, S., Marmo, F., & Rosati, L. (2019a). An accurate and computationally efficient uniaxial phenomenological model for steel and fiber reinforced elastomeric bearings. *Composite Structures*, *211*, 196–212.

Vassiliou, M. F., & Makris, N. (2012). Analysis of the rocking response of rigid blocks standing free on a seismically isolated base. *Earthquake Engineering & Structural Dynamics*, *41*(2), 177–196.

Venanzi, I., Ierimonti, L., & Materazzi, A. L. (2018). Active base isolation of museum artifacts under seismic excitation. *Journal of Earthquake Engineering*, *24*(3), 506–527.

Vestroni, F., & Cinto, S. D. (2000). Base isolation for seismic protection of statues. *Proceedings of 12th World Conference of Earthquake Engineering*, Auckland, New Zealand.

Waltz, R. A., Morales, J. L., Nocedal, J., & Orban, D. (2006). An interior algorithm for nonlinear optimization that combines line search and trust region steps. *Mathematical Programming*, *107*(3), 391–408.

Wen, Y. -K. (1976). Method for random vibration of hysteretic systems. *Journal of the Engineering Mechanics Division*, *102*(2), 249–263.

Wittich, C. E., & Hutchinson, T. C. (2016). Experimental modal analysis and seismic mitigation of statue-pedestal systems. *Journal of Cultural Heritage*, *20*, 641–648.

Yim, C. -S., Chopra, A. K., & Penzien, J. (1980). Rocking response of rigid blocks to earthquakes. *Earthquake Engineering & Structural Dynamics*, *8*(6), 565–587.

Zhang, J., & Makris, N. (2001). Rocking response of free-standing blocks under cycloidal pulses. *Journal of Engineering Mechanics*, *127*(5), 473–483.

Zuccaro, G., Dato, F., Cacace, F., de Gregorio, D., & Sessa, S. (2017). Seismic collapse mechanisms analyses and masonry structures typologies: A possible correlation. *Ingegneria Sismica*, *34*(4), 121–149.

How to cite this article: Pellecchia, D., Lo Feudo, S., Vaiana, N., Dion, J. -L., & Rosati, L. (2021). A procedure to model and design elastomeric-based isolation systems for the seismic protection of rocking art objects. *Comput Aided Civ Inf*, 1–18. https://doi.org/10.1111/mice.12775